



HAL
open science

Nanoscale Analysis of Randall's Plaques by Electron Energy Loss Spectromicroscopy: Insight in Early Biomineral Formation in Human Kidney

Clément Gay, Emmanuel Letavernier, Marie-Christine Verpont, Michael Walls, Dominique Bazin, Michel Daudon, Nadine Nassif, Odile Stéphan, Marta de Frutos

► **To cite this version:**

Clément Gay, Emmanuel Letavernier, Marie-Christine Verpont, Michael Walls, Dominique Bazin, et al.. Nanoscale Analysis of Randall's Plaques by Electron Energy Loss Spectromicroscopy: Insight in Early Biomineral Formation in Human Kidney. ACS Nano, 2020, 14 (2), pp.1823-1836. 10.1021/acsnano.9b07664 . hal-02432794

HAL Id: hal-02432794

<https://hal.sorbonne-universite.fr/hal-02432794>

Submitted on 8 Jan 2020

HAL is a multi-disciplinary open access archive for the deposit and dissemination of scientific research documents, whether they are published or not. The documents may come from teaching and research institutions in France or abroad, or from public or private research centers.

L'archive ouverte pluridisciplinaire **HAL**, est destinée au dépôt et à la diffusion de documents scientifiques de niveau recherche, publiés ou non, émanant des établissements d'enseignement et de recherche français ou étrangers, des laboratoires publics ou privés.

1
2
3
4
5
6
7
8
9
10
11
12
13
14
15
16
17
18
19
20
21
22
23
24
25
26
27
28
29
30
31
32
33
34
35
36
37
38
39
40
41
42
43
44
45
46
47
48
49
50
51
52
53
54
55
56
57
58
59
60

Nanoscale Analysis of Randall's Plaques by Electron Energy Loss Spectromicroscopy: Insight in Early Biomineral Formation in Human Kidney

*Clément Gay*¹, *Emmanuel Letavernier*^{2,3,4}, *Marie-Christine Verpont*^{2,3}, *Michael Walls*¹,
*Dominique Bazin*⁵, *Michel Daudon*^{2,3,4}, *Nadine Nassif*⁶, *Odile Stéphan*¹, *Marta de Frutos*^{1*}

¹ Laboratoire de Physique des Solides, CNRS UMR 8502, Université de Paris-Saclay, F-91405, Orsay, France.

² Sorbonne Université, UPMC Univ Paris 06, UMR S 1155, F-75020, Paris, France

³ INSERM, UMR S 1155, F-75020, Paris, France

⁴ Physiology Unit, APHP, Hôpital Tenon, F-75020, Paris, France

⁵ Laboratoire de Chimie Physique, UMR 8000-CNRS, Université de Paris-Saclay, F-91405 Orsay, France

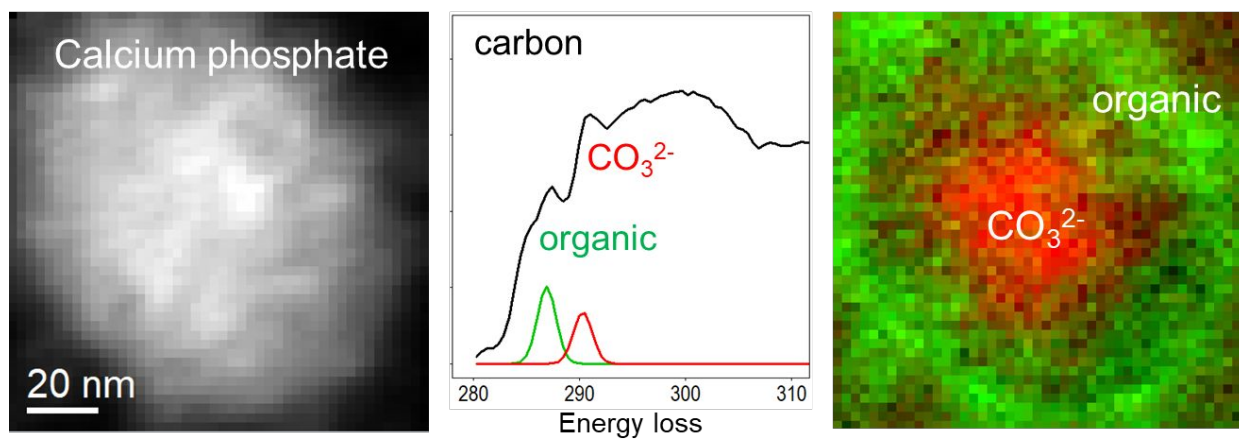
⁶ Sorbonne Université, CNRS, Collège de France, Laboratoire de Chimie de la Matière Condensée de Paris (LCMCP), 4 place Jussieu, F-75005, Paris, France

* Corresponding author: Marta de Frutos

E-mail address: marta.de-frutos@u-psud.fr

ABSTRACT

Idiopathic kidney stones originate mainly from calcium phosphate deposits at the tip of renal papillae, known as Randall's plaques (RPs), also detected in most human kidneys without stones. However, little is known about the mechanisms involved in RP formation. The localization and characterization of such nano-sized objects in the kidney remains a real challenge making their study arduous. This study provides a nanoscale analysis of the chemical composition and morphology of incipient RPs, characterizing in particular the interface between the mineral and the surrounding organic compounds. Relying on data gathered from a calculi collection, the morphology and chemical composition of incipient calcifications in renal tissue was determined using spatially resolved electron energy-loss spectroscopy (EELS). We detected micro-calcifications and individual nano-calcifications found at some distance from the larger ones. Strikingly, concerning the smaller ones, we show that two types of nano-calcifications coexist: calcified organic vesicles and nanometric mineral granules mainly composed of calcium phosphate with carbonate in their core. Interestingly, some of these nano-calcifications present similarities with those reported in physiological bone or pathological cardiovascular biominerals, suggesting possible common formation mechanisms. However the high diversity of these nano-calcifications suggests that several mechanisms may be involved (nucleation on a carbonate core or on organic compounds). In addition, incipient RPs also appear to present specific features at larger scales revealing secondary calcified structures embedded in a fibrillar organic material. Our study proves that analogies exist between physiological and pathological biominerals and provides information to understand the physico-chemical processes involved in pathological calcification formation.



KEYWORDS : Randall's plaques, calcium phosphate nanoparticles, calcium carbonate nanoparticles, kidney, biomineralization, electron energy-loss spectroscopy.

1
2
3 Physiological biominerals such as found in bone and teeth of vertebrates or shells and
4
5 crustacean carapaces of invertebrates, are organized in a hierarchical structure at different
6
7 scales.¹ The organization of the crystal results from a tight control of the mineral deposition *via*
8
9 an interaction with an organic matrix. In many cases, pathological calcifications associated with
10
11 several major diseases such as cancer and cardiovascular abnormalities also appear to be
12
13 organized at the microscale.^{2,3} Of particular relevance is the understanding of how the interface
14
15 between the mineral and the organic compounds regulates the initiation of the calcification
16
17 (nucleation) and the crystal growth at different scales. Different compounds are released from
18
19 the organism preventing the growth or inhibiting the deposition of the mineral at this interface.
20
21 In the context of pathological process, the nucleation and growth of the mineral result from an
22
23 imbalance of these regulation mechanisms.
24
25
26
27
28

29 In kidney, the spatial organization of the mineral phase is frequently linked to the pathology
30
31 at the origin of their formation.^{4,5} Kidney stones show a great chemical diversity^{6,7} but the most
32
33 common composition corresponds to calcium oxalate monohydrate, found in patients without
34
35 any systemic disorder (so-called idiopathic stones). In many cases,^{8–10} these stones originate
36
37 from mineral deposits at the tip of renal papillae known as Randall's plaques (RPs).^{11–13}
38
39 Interestingly, they are not only detected as an anchored site for stone formation in renal-stone-
40
41 forming patients but also in incipient forms in more than two thirds of people without kidney
42
43 stone.¹⁴
44
45
46
47

48 The molecular mechanisms involved in the pathogenesis of RPs are still not known and
49
50 many questions still remain on the formation of such pathological calcifications. Most of the
51
52 RPs structural investigations have been performed at the macroscopic and microscopic scale on
53
54 plaques extracted from kidney stones and characterized by classical FTIR spectroscopy. RPs
55
56 are mainly composed of nanocrystalline carbonated hydroxyapatite and amorphous carbonated
57
58 calcium phosphate but other chemical compounds, such as whitlockite, brushite or monosodium
59
60

1
2
3 urate were also detected.⁹ Moreover, FTIR data show clearly that, in large RPs, apatite presents
4
5 variable levels of carbonation.¹⁵ These observations support the idea that several mechanisms
6
7 may be involved in the pathogenesis of RPs.
8
9

10
11 Compared to physiological biominerals, the investigation of the mechanisms involved in
12
13 the formation of pathological calcifications is particularly challenging because of the limitations
14
15 imposed by working on human specimens. In our work, the strategy was to characterize early
16
17 calcifications in human kidney by a nanoscale analytical approach (electron energy-loss
18
19 spectroscopy) providing data for a direct comparison with other systems more widely studied
20
21 and better understood (*e.g.* bone). Spatially-resolved EELS performed in a STEM (scanning
22
23 transmission electron microscope) provides high spatial resolution elemental maps and allows
24
25 a spectral identification of specific functional groups. Recent studies have proved that EELS
26
27 can be successfully used for the investigation of biominerals by providing highly relevant
28
29 information concerning their formation mechanisms.^{16–20}
30
31
32
33

34
35 Here, incipient RPs from human kidneys were analyzed using Transmission Electron
36
37 Microscope (TEM) and STEM imaging combined with spatially-resolved EELS to improve our
38
39 understanding of the events that precede the pathogenic evolution of RPs. For this purpose, a
40
41 library of EELS fingerprints for RP investigations was built relying on data gathered from a
42
43 calculi collection.⁵ The fact that RPs constitutive elements are nano-sized objects at some
44
45 unknown positions in the kidney makes their localization and characterization arduous,
46
47 restricting advances to understand plaque formation. Because STEM-EELS offers the
48
49 advantage of an outstanding spatial resolution in both imaging and chemical analysis, incipient
50
51 RPs in the renal tissue were successfully localized and analyzed, *i.e.* morphology and chemical
52
53 composition with a nanometer resolution. A high diversity of calcified objects was found in the
54
55 kidney tissue suggesting that RPs formation may be initiated by several mechanisms.
56
57 Interestingly, some of these calcifications present similarities to the structures reported in
58
59
60

1
2
3 physiological bone^{17,21} or pathological biominerals.^{3,22,23} Our study provides information for
4
5 understanding the physico-chemical processes involved in the formation of pathological
6
7 calcifications.
8
9
10
11
12
13
14
15
16
17
18
19
20
21
22
23
24
25
26
27
28
29
30
31
32
33
34
35
36
37
38
39
40
41
42
43
44
45
46
47
48
49
50
51
52
53
54
55
56
57
58
59
60

RESULTS AND DISCUSSION

Localization of incipient calcifications in the kidney tissue

Two samples (from two different patients) were selected among a set of papillae with incipient RPs investigated in a previous study.¹⁴ Papillae were collected from human kidneys removed because of cancer. The samples were taken at some distance from the tumor. They were considered as “healthy” concerning the lithiasic pathology because they were free of stones. The electron microscopy observations (conventional TEM and STEM) of the two specimens reveal, as illustrated in Figures 1 and 2, the presence of two kinds of calcifications: micro-calcifications and individual nano-calcifications found at some distance from the larger ones. A schematic representation of the different classes of detected calcifications is given in Figure 3.

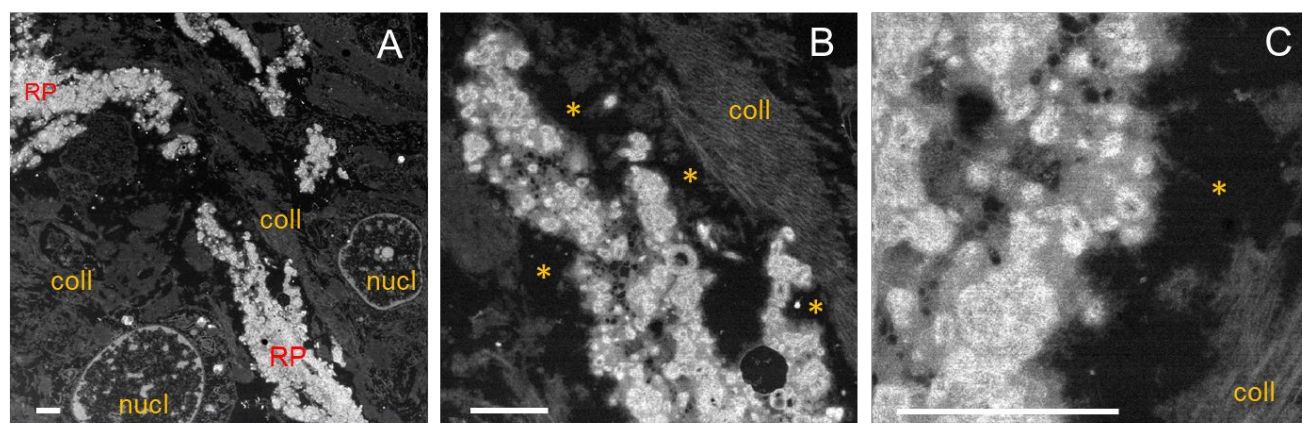


Figure 1: STEM-HAADF images of micro-calcifications. (A) The RPs presented here were located in the interstitium near the urothelium. Cell nucleus (indicated by “nucl”) are visible in the image. Plaques are located in regions rich in collagen (indicated by “coll”) but a gap is frequently observed between the mineral and the collagen fibrils (darkest areas indicated by * in B). A higher magnification (C) shows that RPs are mainly formed by electron-dense objects with rounded shapes connected together by a lower contrast fibrillary network (scale bar = 1 μm).

1
2
3 Micro-calcifications are easily identified as large electron-dense objects in TEM-BF
4 (bright field) and STEM-HAADF (high angle annular dark field) (Figure 1). STEM-HAADF
5 mode gives a contrast corresponding to differences in atomic number and /or local thickness,
6 higher atomic number or thickness appearing brighter. As already described,¹⁴ micro-
7 calcifications were frequently located in collagen-rich regions (indicated by “coll” in Figures
8 1A-C). Collagen is dense and aligns locally (Figure 1B). At higher magnification, a gap is
9 observed between the fibrillar collagen network and the plaques (* in Figure 1B-C). Although
10 artefacts from TEM ultrathin-section preparation cannot be excluded, the fact that this is
11 observed all over the sample tends to show that collagen does not interact intimately with the
12 calcified domains. Figure 1C reveals that micro-calcifications are mainly composed of rounded
13 electron-dense objects interconnected by a disordered fibrillar network. Noticeably, the
14 characteristic co-alignment of bone is not observed.

15
16
17 To get a chance of analyzing the first steps of kidney calcification, further investigations
18 have been performed near the loop of Henle and the *vasa recta*, where some calcifications of
19 nanometer sizes were detected in a previous study.¹⁴ Prior to EELS analysis, specimens were
20 first screened by TEM to establish a map of the grid. More than 200 potential calcifications
21 with granular and vesicle-like shapes were selected in the kidney tissue.

22
23
24 The elemental composition of the selected objects was analyzed by EEL spectroscopy.
25 Typical EEL spectra (Figure 2B) display the characteristic edges of phosphorus (P-L₂₃),
26 uranium (U-O₂₃), carbon (C-K), calcium (Ca-L₂₃), nitrogen (N-K) and oxygen (O-K),
27 respectively at 138, 193, 285, 349, 400 and 531 eV (hydrogen is not detectable by EELS). The
28 appearance of these contributions superposed over the continuously decreasing background is
29 a clear signature of the presence of the element in the specimen foil under the impact of the
30 electron microscope primary beam, of typical size 1 nm.

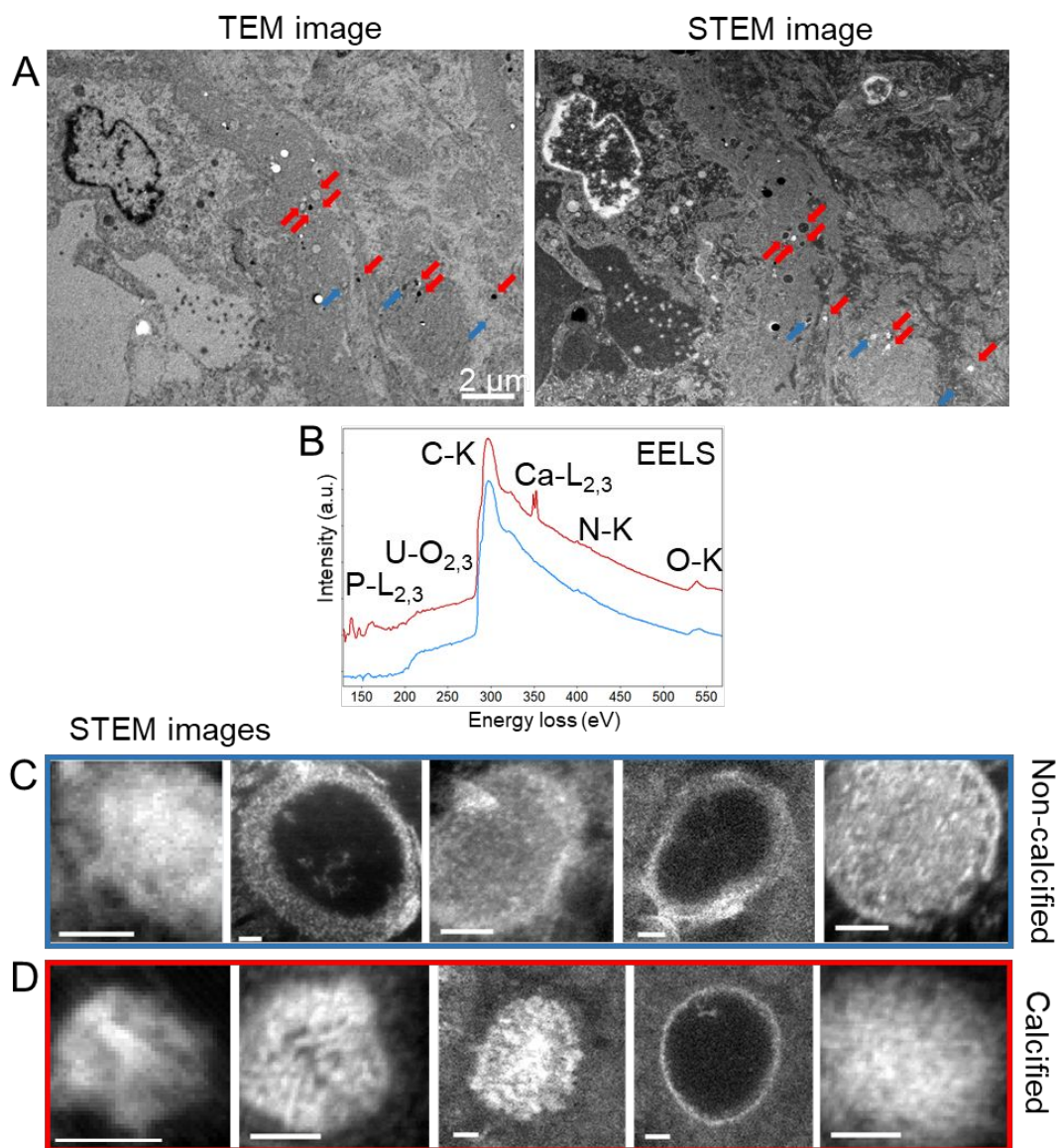


Figure 2: (A) TEM-BF and STEM-HAADF images of a papillae region close to the Henle loop containing potential calcifications (indicated by arrows) appearing as electron-dense objects located in the interstitium. (B) The presence or absence of calcium in the different objects (red curve) allows to distinguish between calcifications (red arrows in A, STEM-HAADF images in D) from non-calcified objects (blue arrows in A, STEM-HAADF images in C) (Scale bar in C) and D) = 50 nm).

Among the 200 selected objects, about 25% are found to contain calcium (red curve in Figure 2B). The remaining fraction is formed from undetermined biomolecules (proteins, nucleic acids, lipids) as revealed by the presence of nitrogen, able to fix the staining contrast (blue curve). In Figures 2C and D, the differences in composition emphasize that these nano-calcifications cannot be identified on purely morphological criteria, from electron-dense

1
2
3 structures fixing contrast agent. Of note, most of the extracellular rounded, electron-dense,
4 nanometric structures are not calcifications (Figure 2A, blue arrows compared to red ones).
5 Hence, this result highlights the limitations of the methodology based on TEM images for
6 identifying calcifications and defining their organic/mineral interface.^{24,25} It is essential to carry
7 out elemental analysis at the nanometer scale.
8
9
10
11
12
13
14
15
16
17

18 **Morphology of the incipient calcifications and their elemental distributions**

19
20
21 In our experiments, the whole EELS data set was acquired in the spectrum-imaging
22 mode: the focused electron beam of the STEM was scanned over the area of interest and an
23 EEL spectrum was recorded for each position simultaneously with the HAADF image.
24 Therefore elemental maps corresponding to the distribution of phosphorus, calcium and
25 nitrogen are then obtained from the EEL spectrum by integrating the intensity of the respective
26 edges after background subtraction in front of every edge according to the standard EELS
27 methodology. The 1 nm probe diameter sets the spatial resolution of the maps.
28
29
30
31
32
33
34
35
36
37

38 Micro-calcifications are made of calcium phosphate particles associated with organic
39 material (Figure 3B-E). The spatial variation of the composition may explain the contrast in the
40 HAADF images as mentioned above. For the nano-calcifications, the elemental maps show
41 that, in most cases (~ 90 %), phosphorus is associated with calcium (Figure 3F-I) but a minority
42 of calcifications is composed of pure calcium carbonate (Figure 7D).
43
44
45
46
47
48
49
50
51
52
53
54
55
56
57
58
59
60

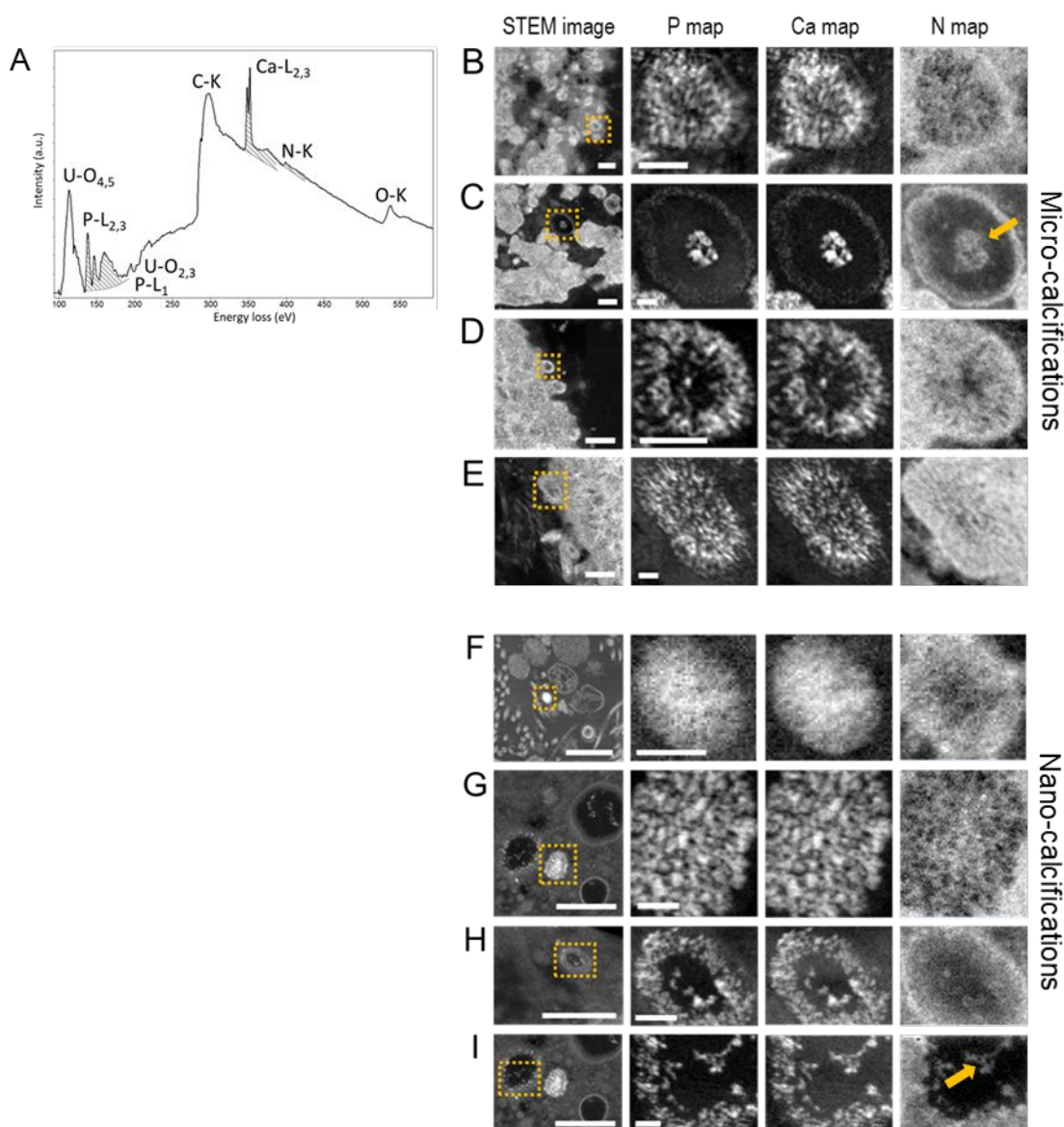
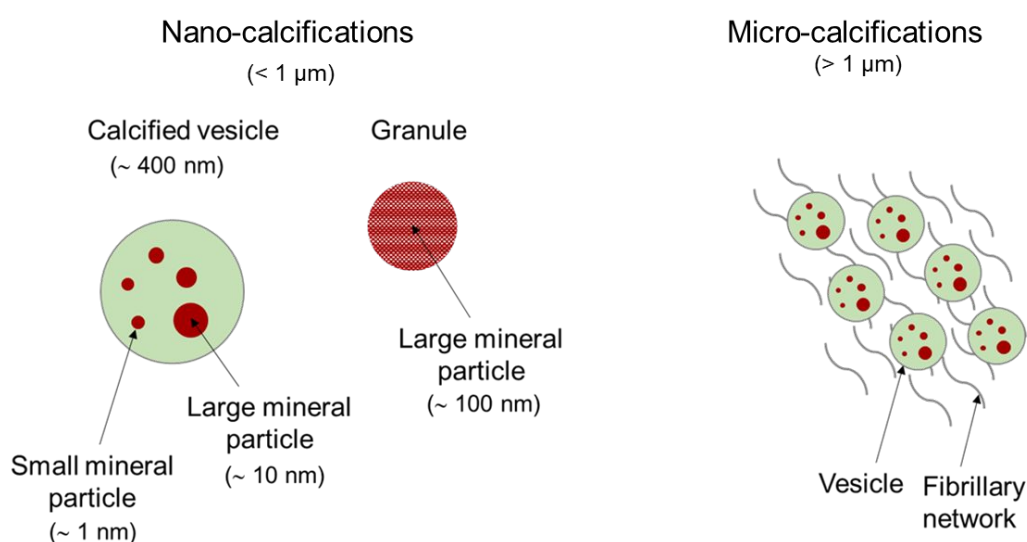


Figure 3: (A) Typical EEL spectrum acquired on a calcification made of calcium phosphate (Ca and P $L_{2,3}$ edges are visible). Carbon and nitrogen (K-edges) associated with the presence of organic material and resin are also detected. EELS maps are obtained from the intensity sum of the corresponding edge after background subtraction (the dashed area is a schematic representation of background modelling). Maps showing the distribution of P, Ca and N for the different calcified objects in the areas delimited by yellow squares in the respective STEM images: for micro- (B-E) and nano-calcifications (F-I). Mineral particles are detected by the signal of calcium and phosphate (P and Ca maps) and are associated with organic compounds as revealed by the presence of nitrogen (N map) (yellow arrows in C and I). They are assembled together to form objects with very diverse morphologies and sizes (see main text for details). Scale bar = to 500 nm for STEM-HAADF images and 50 nm for EELS maps.

1
2
3 Considering all the calcified objects (nano- and micro-calcifications represented
4 schematically in Figure 4), the mineral is found in particles with sizes that can be classified into
5 two main groups: small particles (few nm approximately) and large particles (from few tens to
6 250 nm with an average of ~100 nm). Small mineral particles (small MPs) assemble forming
7 objects with different morphology and size. Large mineral particles (large MPs) present a fairly
8 homogeneous distribution of calcium (Figure 3F) and are mostly found at distance from micro-
9 calcifications. Some hybrid structures are found to contain both small and large MPs (about 50
10 nm) (Figure 3C). The presence of isolated small MPs cannot be excluded but they would be
11 difficult to locate with our methods.
12
13
14
15
16
17
18
19
20
21
22
23
24
25
26
27
28
29
30
31
32
33
34
35
36
37
38
39
40
41
42
43
44



45 **Figure 4:** Schematic representations of the different classes of calcified objects found in kidney.
46 Red circles represent the mineral particles and green ones the organic components. Nano-
47 calcifications correspond to sub-micrometric objects made of a single mineral particle or of a
48 vesicle enclosing several mineral particles (MP). MPs are classified into two main groups: with
49 sizes under 10 nm, designated as “small” and particles of a few tens to about 250nm,
50 designated as “large”. Micro-calcifications are large calcified objects (several micrometers)
51 mainly composed of calcified vesicles interconnected by a disordered fibrillar network
52 represented by gray wavy lines.
53
54
55
56
57
58
59
60

1
2
3 Nitrogen and calcium maps give the distribution of the organic and mineral compounds and
4 allow one to characterize the detailed relationship between organic and mineral phases, *i.e.* the
5 organic/mineral interface. In most cases, the assemblies containing small MPs are surrounded
6 by an organic envelope (Figure 3B, C, D, E, H and I). In these vesicle-like structures, MPs are
7 visible in close contact with the membrane inner surface or in the vesicle center (Figure 3C, H
8 and I). For the particles located in the center of the vesicles, organic compounds are detected
9 on the nitrogen maps associated with the mineral (arrows in Figure 3C and I). An apparent
10 diameter from 100 to 700 nm (400 nm on average) is measured for vesicles but this value may
11 be an underestimation if the resin section doesn't cross the center of the sphere. In few cases,
12 small MPs are also detected embedded in an organic matrix to form assemblies with no visible
13 membrane around them (Figure 3G). This can be observed when the calcified vesicle is cut
14 close to its surface.
15
16
17
18
19
20
21
22
23
24
25
26
27
28
29
30

31 To further elucidate the chemical composition of the calcifications, we performed energy
32 dispersive X-ray (EDX) analysis. A typical spectrum is presented in Figure 5. As expected,
33 phosphorus and calcium were detected as the major elements composing the micro- and nano-
34 calcifications. The spectra show peaks (labeled by * in Figure 5A) associated with the copper
35 from the TEM grid and the staining elements (osmium, lead and uranium). Small amounts of
36 silicon and fluorine were found. Other elements reported in previous biomineral studies (Mg,
37 Na, K, Fe)¹⁹ were not detected in our analysis. The Ca/P ratio (atomic %) is within the range
38 (1.30 -1.50) (estimated error of 0.15) for microcalcifications whereas it is lower for
39 nanocalcifications between 0.9 and 1.4 (estimated error of 0.2). Figure 5B corresponds to a
40 region where a microcalcification, calcified vesicles containing small MPs and large MPs are
41 present. The areas delimited by a yellow (or red) line have a Ca/P ratio below (or above) 1.3.
42 In the literature, values between 1.2 and 2.2 are reported for ACP and between 1.5 and 1.67 for
43 calcium-deficient HA.^{26,27} In our present study, the low Ca/P ratio may indicate the presence of
44
45
46
47
48
49
50
51
52
53
54
55
56
57
58
59
60

such phases. However, the fact that the sample contains a significant amount of organic material and that a mixture of mineral phases cannot be discarded, the identification of the phases can only be proposed. Note that the low values observed for the calcified vesicles are likely to be associated to the presence of organic phosphates.

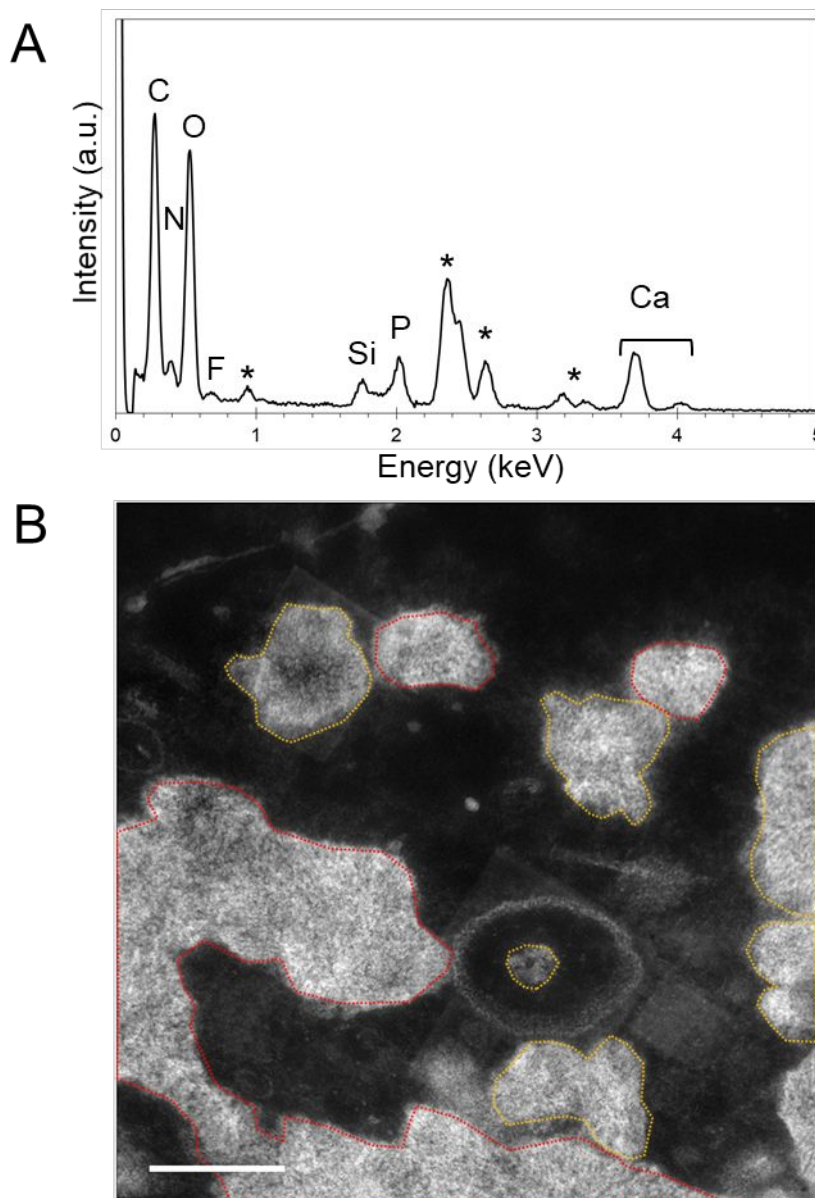


Figure 5: (A) Typical EDX spectrum acquired from the area presented in HAADF image (B). Carbon (C), nitrogen (N), oxygen (O), phosphorus (P) and calcium (Ca) are clearly detected in all areas together with small traces of silicon (Si) and fluorine (F). The peaks labeled by (*) are associated with the copper from the grid and the elements used to stain the specimen (osmium, lead and uranium). The Ca/P ratio varies from 0.9 to 1.5. Areas are delimited by a yellow dotted line for a value below 1.3 and by a red one above 1.3. Scale bar = 300 nm.

1
2
3 In order to further analyze the mineral composition of the calcifications, the fine structure
4 of the elemental edges was compared with a library of EELS signatures obtained from kidney
5 stones, pure minerals and organic references.
6
7
8
9

14 **Building a library of EELS fingerprints for refined chemical analysis**

17 In order to gain more information about the chemistry of the nanocalcifications, we
18 selected for comparison three macroscopic kidney stones representative of the main
19 compositions previously reported for incipient RPs¹⁴ among the abundant calculi collection
20 (more than 85,000) from Tenon hospital.⁵ These stones were mainly composed of carbonated
21 hydroxyapatite (CHA), amorphous carbonated calcium phosphate (ACCP) and whitlockite
22 (WK) as shown by FTIR spectroscopy (Figure S1). In addition to the composition of kidney
23 stones, FTIR spectroscopy was useful to estimate their content in minerals and organic
24 compounds (proteins for instance) as described in previous studies.⁵ For the samples used in
25 the present study, 20 wt% proteins was found in WK, 2 wt% in CHA and 10 wt% of proteins
26 in ACCP.
27
28
29
30
31
32
33
34
35
36
37
38
39
40

41 The different kidney stones were then analyzed by EELS. Beam-induced damage was
42 assessed by recording spectra for doses from 2×10^5 to 6×10^7 e⁻/nm². The dose was chosen
43 between 5×10^6 and 10^7 e⁻/nm² for the acquisitions in order to achieve a good signal-to-noise
44 ratio allowing an optimized identification for both minerals and organic compounds (Figure S2
45 and S3). At such doses, the organic compounds are clearly discriminated from the embedding
46 resin. The stone edge signatures (Figure 6E-H) were compared with the fingerprints of pure
47 mineral references (synthetic hydroxyapatite, HA, and calcite, CAL, Figure 6A-D) and of
48 organic compounds (Figure S4).
49
50
51
52
53
54
55
56
57
58
59
60

EELS data were acquired in the spectrum-imaging mode but the spectra presented in Figure 6 come from a point analysis at a fixed localization on the sample determined by the position of the microscope electron beam. In contrast to the FTIR data that correspond to average compositions at the macroscopic scale, the EEL spectra are very sensitive to the probe position, revealing the specimen heterogeneity: for instance, proteins are visible in some areas and absent from others. The data reported here correspond to some common features observed for each sample but do not reflect the average content of the stones.

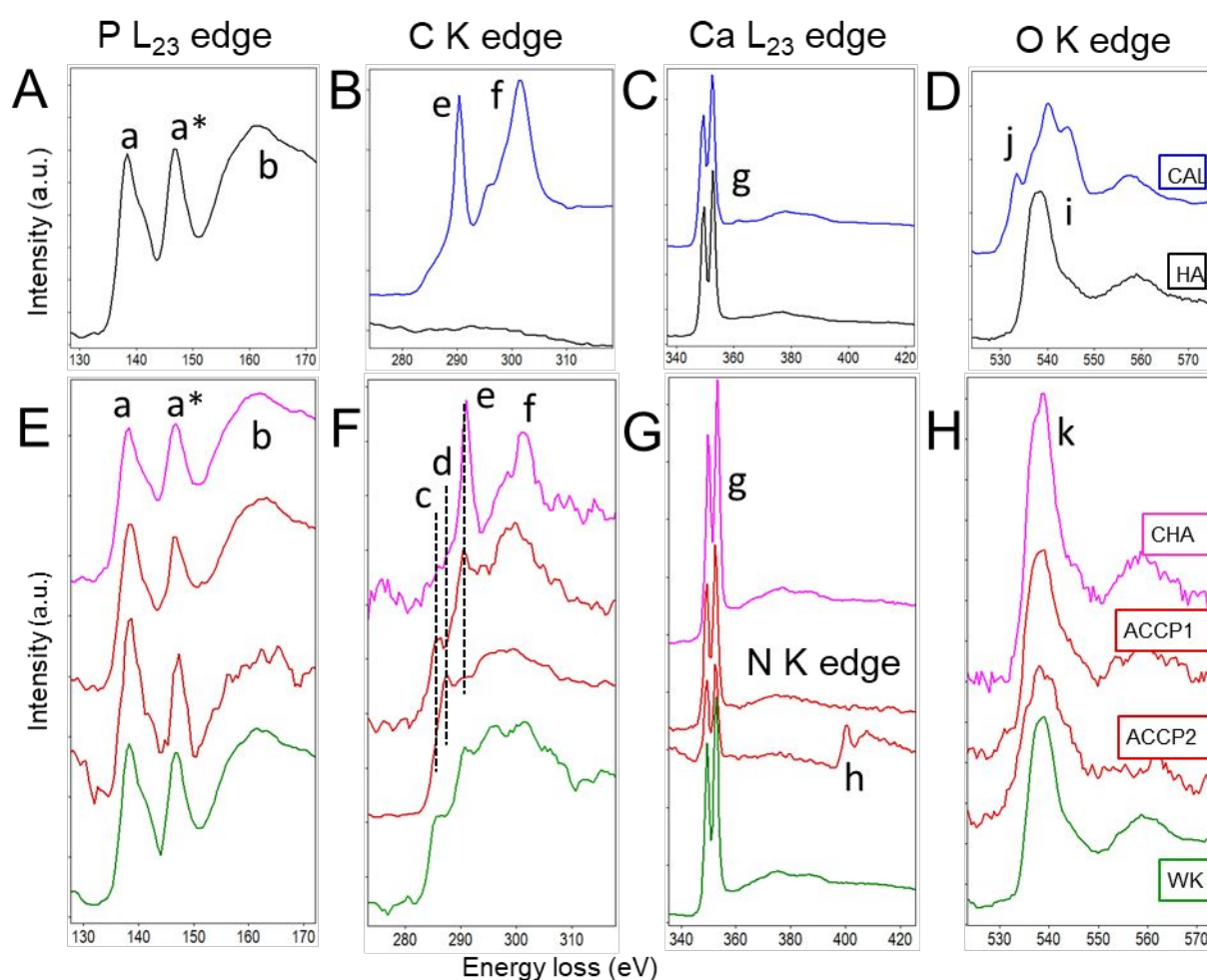


Figure 6: EEL spectra associated with the phosphorus, carbon, calcium, nitrogen and oxygen edges acquired on hydroxyapatite (HA), calcite (CAL) and on kidney stones composed of CHA, ACCP and WK. Spectra are presented in: (A-D) for HA and CAL by the black and blue curves respectively; (E-H) for CHA, ACCP and WK by the purple, red and green curves respectively. These spectra have been acquired for a fixed localization on the samples determined by the position of the microscope electron beam. The assignment of the EELS features for mineral and organic compounds is given in Table S1.

1
2
3
4
5
6 Our data are compatible with previous studies based on X-ray absorption experiments
7
8 on the same type of compounds²⁶ that provide information with a better spectral resolution than
9
10 EELS. The energy scale of EEL spectra is calibrated according to XANES analysis from²⁶
11
12 using the peak maximum positions of the phosphorus and calcium L₂₃ edges, respectively at
13
14 138 eV and 349 eV. These features are chosen due to their negligible variation in position for
15
16 the different calcium phosphate compounds as demonstrated in previous studies.²⁸ For pure
17
18 calcium carbonate, the carbonate peak of the carbon K edge at 290 eV is alternatively used for
19
20 the calibration together with the calcium peaks. Peak assignments (annotated *a* to *k* in Figure
21
22 6) and energy loss characteristic of the different compounds are summarized in Table S1.
23
24
25

26
27 For the reference CAL, the main characteristic features are two peaks for the carbon K
28
29 edge at 290 and 301 eV assigned to the carbonate group (labeled *e, f* in Figure 6B) and a set of
30
31 four peaks for the oxygen K edge (labeled *j* in Figure 6D).^{29,30} HA's principal features are three
32
33 peaks for the phosphorus L₂₃ edge (labeled *a, a** and *b* in Figure 6A), a double peak for the
34
35 calcium L₂₃ edge (labeled *g* in Figure 6C) and the oxygen K edge exhibits only a double peak
36
37 unresolved at our energy resolution (labeled *i* in Figure 6D).^{31,32}
38
39
40

41
42 In calcium phosphate compounds identified by FTIR in the kidney stones, the exact
43
44 peak pattern (number, position and intensity of small peaks) of the P- and Ca-L₂₃ edges is
45
46 specific to each compound^{33,34} because it is determined by the crystal field resulting from the
47
48 atomic arrangement.³⁵ But the limited energy resolution in our measurements (about 1 eV) does
49
50 not give access to such detailed information as evidenced by the similarity of the phosphorus
51
52 and calcium edges for CHA, WK and ACCP (Figure 6E and G) to those for pure HA (Figure
53
54 6A and C) and the similar appearance of Ca edge for HA and calcite. Although the features are
55
56
57
58
59
60

1
2
3 not sensitive to the crystallinity, calcium phosphate (CaP) and calcium carbonate are easily
4
5 distinguishable.
6
7

8
9 The nitrogen signal (denoted *h* in Figure 6G) together with the peak at ~ 287 eV in the
10
11 carbon K edge (peak *d* in Figure 6F) are features compatible with the presence of the proteins
12
13 detected by FTIR (20 wt % in WK, 2 wt % in CHA and 10 wt % in ACCP). At some positions,
14
15 peaks are also detected at ~285 eV and at ~290 eV (respectively peaks *c* and *e* in Figure 6F)
16
17 indicating the presence of amorphous carbon and carbonate respectively. The peak at 285 eV
18
19 may be related, at least partially, to radiation-induced damage on organic compounds as already
20
21 reported³⁶ (details in SI).
22
23
24

25
26 The oxygen K edge (peak *k* in Figure 6H) results from the contributions of mineral
27
28 (phosphate and carbonate) (Figure 6D) and organic compounds (Figure S4C). As previously
29
30 reported,¹⁶ the presence of hydroxyl group cannot be detected on oxygen edge in EELS analysis.
31
32 The oxygen edge is similar for WK, HA, and CHA when only a small amount of carbonate is
33
34 present. For ACCP, its shape varies with the position on the stone specimen, turning from HA-
35
36 like (ACCP1 in Figure 6H) to a more triangular shape (ACCP2 in Figure 6H). This triangular
37
38 shape is always associated with a nitrogen signal and a carbon peak at 287 eV revealing the
39
40 presence of the proteins at this position.
41
42
43

44
45 This rich chemical information conveyed by the fine structures on the characteristic EELS
46
47 edges from Ca phosphate and carbonate references forms then the basis for the subsequent
48
49 EELS analysis on incipient RPs.
50
51
52
53
54

55 **Refined chemical analysis of the incipient calcifications.**

56
57
58
59
60

1
2
3 The fine structure of the elemental edges on kidney calcifications (Figure 7A-D) was
4 compared with the library of EELS signatures obtained from the macroscopic kidney stones,
5 pure minerals and organic references (Figures 6 and S4 respectively). Unstained papillae
6 specimens have also been analyzed in order to exclude a possible contribution from staining
7 compounds and no difference was found. Papillae specimens contain three types of compounds:
8 the mineral, the biomolecules composing the kidney tissue (designated from here on as “organic
9 compounds”) and the embedding resin. The exact nature of the biomolecules found in the
10 specimen is hard to determine from spectroscopic data alone. However, organic compounds are
11 clearly discriminated from the resin by examining the features of carbon, nitrogen and oxygen
12 edges (see details in SI). The presence of organic compounds in the biomineral is revealed by
13 a peak at ~287 eV on the carbon K edge (Figure 7, peak *d*) in correlation with the presence of
14 nitrogen (Figure 7, peak *h* at 400 eV). The peak at ~ 285 eV (Figure 7, peak *c*) is detected on
15 the carbon edge mostly due to the presence of the epoxy resin (Figure S5A and details in SI).
16 There is no carbon support film contribution to the EELS spectra since the resin sections were
17 deposited on bare copper grids.
18
19
20
21
22
23
24
25
26
27
28
29
30
31
32
33
34
35
36
37

38 Two main mineral compounds are detected in the particles: calcium carbonate and
39 calcium phosphate, easily distinguishable *via* the phosphorus, carbon and oxygen signals. The
40 MP’ mineral compositions are summarized in Table 1 for small and large MPs.
41
42
43
44
45
46
47
48
49

50 **Composition of Mineral Particles**

Small MPs (<10 nm) In 25 objects	88% pure calcium phosphate 12% calcium phosphate + carbonate
Large MPs (>10 nm to 250 nm) In 27 objects	8% pure calcium carbonate 60% calcium phosphate + carbonate 32% pure calcium phosphate

Table 1

Small MPs are mainly composed of calcium phosphate (~90%) and their EELS features (red curves in Figure 7) are very similar to ACCP. When the carbon peak at 287 eV is detected (Figure 7, peak *d* for C edge), the oxygen edge exhibits the same triangular shape observed for ACCP containing proteins (ACCP2 in Figure 6H) and a nitrogen signal is visible.

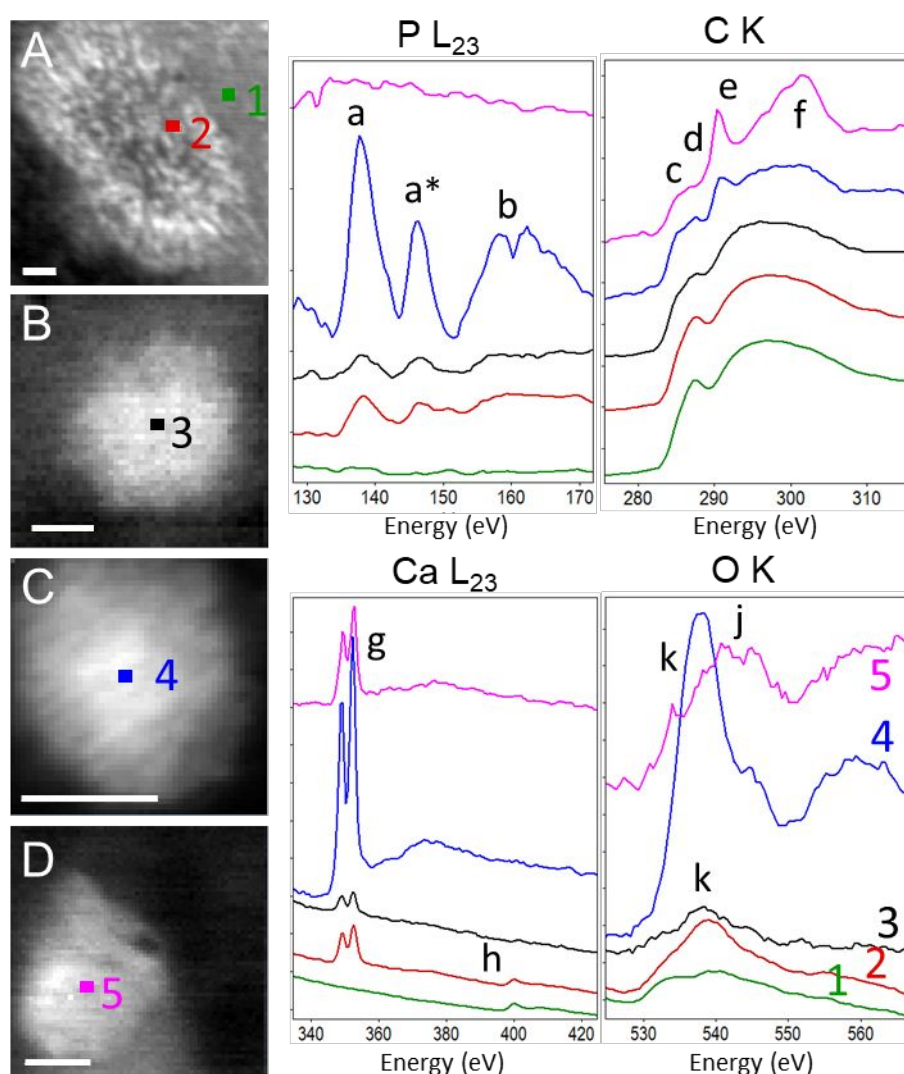


Figure 7: Edge features for different calcifications: red curves are associated with small MPs enclosed in a vesicle for the position indicated by the red square in the HAADF image A; black and blue curves correspond to large MPs made of calcium phosphate (respectively black and blue squares in B and C); purple curves correspond to a large MPs made of pure calcium

carbonate (purple square in D). For comparison, the green curves correspond to organic material and resin (green square in A). Scale bar = 50 nm.

The analysis of large MPs (~ 100 nm) shows that the main component is calcium phosphate (~90% of large MPs) and more rarely calcium carbonate (~10% of large MPs). Among large calcium phosphate MPs, approximately two thirds were found to contain variable amounts of carbonate in their cores (Figure 7, peak *e* on purple curve), sometimes as traces (for instance on blue curve). Calcium phosphate MPs with no detectable carbonate (or small quantities) contained significant amounts of organic compounds as revealed by the presence of the carbon peak at 287 eV (Figure 7, peak *d* on black curve).

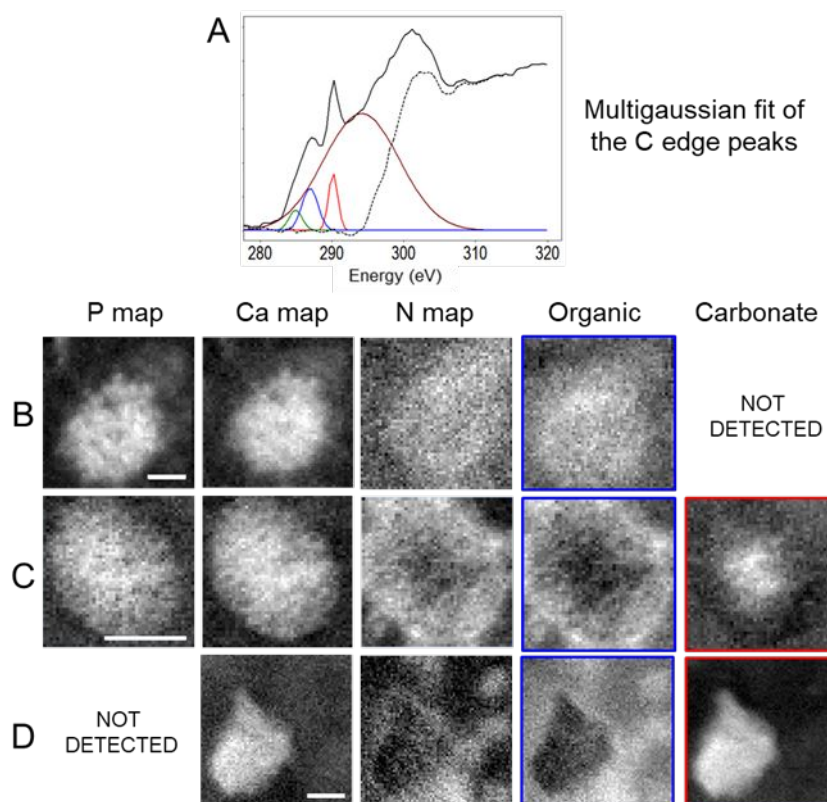


Figure 8: Phosphorus, calcium and nitrogen maps for the large MPs presented in Figure 7 and some ones composed of pure calcium phosphate (B) calcium phosphate and carbonate (C) and calcium carbonate (D). The distributions of amorphous carbon, organic compounds and carbonate are obtained by fitting the peaks at 285 eV, 287 eV and 290 eV on C K edge (respectively green, blue and red Gaussians in figure A). A fourth Gaussian (brown curve) is used to fit the carbon σ^* peak. The dotted line gives the difference between the experimental data and the sum of the four Gaussians. The maps “Organic” and “Carbonate” in figures B-

1
2
3 *D correspond to the Gaussian amplitude associated with the fit of the 287 eV and 290 eV peaks.*
4 *Scale bar = 50 nm.*
5
6
7
8

9 The nitrogen signal allows the detection of organic compounds even if its low intensity
10 makes it harder to map low concentrations. Alternatively, the presence of organic compounds
11 is more easily detected by probing the peak *d* at 287 eV on the carbon edge. For large MPs, the
12 peaks on C edge can be processed by performing a multi-Gaussian fitting. At a given pixel
13 spatial position, each peak associated with a functional group (at 285, 287 and 290 eV for
14 amorphous carbon, organic compounds and carbonate group, respectively) is fitted by a
15 Gaussian (Figure 8A). A fourth Gaussian is used to fit the carbon σ^* peak that is always present.
16 The Gaussian amplitude across the analysed area (Gaussian position and width were kept
17 constant) gives then the relative abundance of the respective functional group. In the examples
18 presented in Figure 8, the maps obtained from the Gaussian fitting of the 287 eV peak (blue
19 Gaussian giving the “Organic” map in Figure 8) are in good agreement with the nitrogen maps
20 (“N map” in Figure 8) confirming that both features are associated with the same compound(s).
21
22
23
24
25
26
27
28
29
30
31
32
33
34
35
36

37 For pure calcium phosphate MPs (Figure 8B), organic compounds are detected both
38 inside and around the particle suggesting that they are intimately associated with the mineral.
39 The carbonate peak at 290 eV (red Gaussian giving the “Carbonate” map in Figure 8) was
40 obviously detected in pure calcium carbonate MPs (Figure 8D) but more interestingly, calcium
41 carbonate formed the core of certain calcium phosphate particles (Figure 8C). When carbonate
42 is present in either of these cases, the organic compound is localized around the carbonate, with
43 negligible overlap (Figures 8C and D).
44
45
46
47
48
49
50
51
52
53

54 In Figure 7, the edge intensities for the different compounds are normalized in order to
55 have a constant value for the carbon signal integrated between 280 and 310 eV. Interestingly,
56 calcium phosphate MPs with no carbonate (or small quantities) most often contain a fairly low
57
58
59
60

1
2
3 amount of calcium (Figure 7B, black curve) . By contrast, calcium phosphate MPs with high
4
5 amounts of carbonate and pure calcium carbonate MPs contain larger amounts of calcium
6
7 (Figure 7C). Pure calcium carbonate MPs do not contain organic compounds in their core (or
8
9 only small quantities) (Figures 7D and 8D). The carbonate peak is rarely present in small MPs
10
11 particles (Figure 7A) and is only detected in some MPs of intermediate size (~ few tenth of
12
13 nm). However the presence in smaller MPs of small amounts of carbonate under the detection
14
15 limit cannot be excluded.
16
17
18
19

20 Our results show that a negligible amount of organic material is detected with calcium
21
22 carbonate in contrast to calcium phosphate which is always associated with a high organic
23
24 signal. Such a difference may be related to the particle size of biogenic calcium carbonate (*e.g.*
25
26 micro-sized aragonite platelets in nacre) that is larger than that of calcium phosphate (*e.g.*
27
28 nano-sized apatite platelets in bone).³⁷ Smaller crystals expose more surface area increasing
29
30 possibly mineral-organic interactions that may preclude further crystallization steps by
31
32 screening the calcium. This may explain why calcium carbonate contains a higher amount of
33
34 calcium compared to calcium phosphate.
35
36
37

38 Overall, our observations suggest that different mechanisms are at the origin of the
39
40 formation of the two classes of mineral particles.
41
42
43
44
45
46

47 **Nano-calcifications share similarities with the transient mineral species found** 48 **in other calcified tissues** 49 50

51
52
53 The observed nano-calcifications (large MPs ~100 nm or organic vesicles ~400 nm
54
55 containing small MPs) remind in terms of morphology and composition the calcified
56
57 amorphous precursors and the membrane vesicles (MVs) containing mineral reported for some
58
59
60

1
2
3 calcified tissues.^{21,38–40} Both kinds of objects are proposed as transient mineral species during
4
5 the early mineralization stages but have not yet been generally accepted. In particular, it should
6
7 be emphasized that the nature of MVs is still under debate but they are described to form from
8
9 the cell membrane (of cartilage or bone-forming cells) within whose enclosed spaces the
10
11 nanocrystals of Ca–inorganic phosphate (Pi) are deposited.⁴¹ Mineral precursors are usually
12
13 described as an unstable and disordered colloidal phase that transforms into the more stable
14
15 mature crystal.^{21,30,38,42} In contrast, MVs are only observed during early physiological
16
17 osteogenesis.³⁹ They may be involved in the initiation of calcification by regulating the
18
19 extracellular concentrations of mineral inhibitors (pyrophosphates) and promoters (Pi) and by
20
21 acting as mineral nucleation sites.⁴¹ Interestingly, a defect in systemic pyrophosphate synthesis
22
23 has been recently proposed as a major determinant of RPs formation.⁴³ Several studies have
24
25 suggested during the last few years that an osteoblast-like mechanism is responsible for
26
27 pathological calcifications found in blood vessels and cartilage, and for those related to
28
29 cancer.^{3,22,23} Interestingly, MVs have been described for the pathological calcifications
30
31 associated with *e.g.* osteoarthritis, atherosclerosis, arteriosclerosis and tumors.^{22,23} Concerning
32
33 kidney calcifications, the relation with bone apatite formation was evoked in several studies
34
35 and some authors suggest that renal epithelial cells have the capacity to become osteogenic
36
37 ^{24,44,45} but until now, no direct evidence has been provided for this.

38
39
40
41
42
43
44
45 What information can we deduce from the above observations on the localization,
46
47 morphology, elemental and chemical analysis of the different families of calcified objects in
48
49 kidney?
50

51
52
53
54 **Nucleation can be driven by a carbonate core acting as a bioseed or by organic**
55 **compounds.**
56
57
58
59
60

1
2
3 Amorphous calcium phosphate (ACP) particles with sizes ~ 80 nm have been described
4
5 as transient mineral precursors for bone formation in some living organisms.^{21,38,46} In the
6
7 present study, the large MPs have sizes (~ 100 nm) and morphologies close to these bone
8
9 mineral precursors. However their crystallinity cannot be assessed because the protocol used
10
11 for specimen preparation implies their dehydration and does not guarantee a preservation of the
12
13 mineral crystallinity:¹⁸ amorphous phases are thermodynamically unstable, and easily
14
15 transform into crystalline phases. Large MPs are mainly composed of calcium phosphate but
16
17 variable amounts of carbonate are found in the core of more than 50% of the large MPs. 8% of
18
19 MPs were composed of pure calcium carbonate without phosphate. Calcium phosphate
20
21 compounds are known to be less soluble than calcium carbonate and it was shown that the
22
23 presence of carbonate in solution increases the hydroxyapatite solubility⁴⁷ decreasing the size
24
25 of the particles.⁴⁸ However, similarly to the large MPs observed in our samples, carbonate was
26
27 recently detected in the core of bone mineral precursors leading the authors to suggest that
28
29 calcium carbonate deposits could act as bioseeds for calcium phosphate deposition.¹⁷
30
31 Furthermore, the exposition of human osteogenic cells to bicarbonate seems to enhance the
32
33 calcium phosphate deposition and this stimulation was attributed to the activity of the carbonic
34
35 anhydrase present in MVs.⁴⁹ These observations are meaningful for kidney where the calcium
36
37 concentration is predicted to be extremely high in the interstitial tissue at the papilla tip:⁵⁰
38
39 carbonic anhydrase II is found in most kidney segments and plays an important role in renal
40
41 physiology.⁵¹ Moreover, an acid excretion occurs in the distal part of the nephron and alpha-
42
43 intercalated cells excrete bicarbonate toward the interstitium through anion exchangers,
44
45 potentially increasing bicarbonate content locally.⁵² High calcium and bicarbonate
46
47 concentrations may therefore increase locally to a level of supersaturation that promote
48
49 carbonate granule formation. Carbonate is present in biological apatites (enamel, dentin, bone,
50
51 and pathological calcifications) by substitution at phosphate and hydroxide sites and the
52
53
54
55
56
57
58
59
60

1
2
3 presence of highly carbonated apatite in macroscopic RPs was previously reported but the role
4 of carbonate-rich deposits acting as an initial site for the calcium deposition was never described
5
6 in this context.^{14,53}
7
8
9

10
11
12
13 A different mechanism of nucleation may occur for large MPs where carbonate is not
14 detected (or only traces) in their core and for the small MPs. For these large MPs, high amounts
15 of organic compounds are found in their cores (Figure 8B). Similarly, for the small MPs,
16 organic compounds are also found associated with the mineral (arrows in Figure 3C and I). For
17 a nucleation driven by organic compounds, it is described to occur through different
18 mechanisms in the bone literature including (i) entrapment of mineral's precursor ions inside
19 the confined space of a small pore,⁵⁴ leading to a local increase of ions concentration (reaching
20 the supersaturation) and/or (ii) by a crystallographic match between the protein binding
21 moieties and the calcium (heteroepitaxy).⁵⁵ Similar processes may occur here. The size of the
22 MP depends on the balance between the nucleation and growth processes: high local
23 concentrations of proteins may favor the formation of abundant nuclei at the expense of the
24 crystal growth due to a local depletion of the mineral ions. Many proteins have been identified
25 in the RPs from stone formers suggesting a role in the pathological evolution.⁵⁶
26
27
28
29
30
31
32
33
34
35
36
37
38
39
40
41
42
43
44
45

46 **Calcified vesicles as building blocks of Randall's plaques**

47
48
49

50 The most striking objects observed here are vesicle-like objects containing MPs (Figure
51 4). Strong variations were reported in MV sizes for different systems.⁵⁷ The present values (~
52 400 nm on average) are close to the data reported on mouse osteoblasts using cryo-electron
53 microscopy showing MPs in close contact with the MV inner surface, often interconnected by
54 fibrillary structures.⁴⁰ The calcified vesicles found here appear very similar, with the difference
55
56
57
58
59
60

1
2
3 that the MPs are smaller in size (from a few nm to 50 nm approximately *versus* 80 nm). The
4
5 same authors have shown that MVs in adult zebrafish bones are smaller and the mineral does
6
7 not appear to be organized into 80 nm granules.⁵⁸ MPs connected by fibrils closely resembling
8
9 the ones seen here were also found enclosed in MVs in cultured human vascular smooth muscle
10
11 cells in the absence of Fetuin-A.⁵⁹ MVs are composed of anionic-phospholipids and contain
12
13 numerous proteins.^{57,60} Phospholipids are able to interact with calcium phosphate and to induce
14
15 *in vitro* apatite precipitation.^{41,61,62} Hence, the MVs' ability to nucleate calcium phosphate could
16
17 explain why the inner surface of the kidney calcified vesicles is in many cases enriched in
18
19 mineral particles.
20
21
22
23

24
25 The calcified vesicles were observed as individual objects (Figure 3G-I) but also
26
27 clustered together forming micro-calcifications by interaction with an organic fibrillary
28
29 network (Figures 1 and 3B-E). This observation suggests that calcified vesicles could
30
31 correspond to the initial stages of the formation of the RPs. In many calcified tissues (bone,
32
33 dentin, cementum, pathological cartilage), the organic network is mainly composed of collagen
34
35 that constitutes the scaffold for mineral deposition.⁶³ In cardiovascular tissues, spherical
36
37 mineral particles are associated with collagen fibrils to form macroscopic vascular lesions in an
38
39 architecture distinct from bone material.³ Here, in the less dense regions of the micro-
40
41 calcifications, ramified structures are observed between calcified vesicles (Figure 1C). Fibrils
42
43 are thinner than the collagen ones (indicated by "coll" in Figure 1C) and not organized. They
44
45 are not striated and the mineral does not co-align in a preferential direction as described in bone.
46
47 Moreover, although incipient calcifications are always found in collagen-rich regions, further
48
49 observations show a gap between the collagen fibers and the calcified hybrid domain (* in
50
51 Figures 1B-C). These observations tend to rule out the presence of collagen fibers at the first
52
53 stages of RP formation (Figure 1A and B) while other fibrillar proteins may be involved, such
54
55 as elastin.^{60,64}
56
57
58
59
60

1
2
3 In a recent study concerning cardiovascular pathologies, “spherical mineral particles”
4
5 were detected forming certain calcifications but also in non-calcified areas of tissues at some
6
7 distance from the lesions.³ More surprisingly, they were found even in the absence of
8
9 macroscopic pathological lesions in about 50% of aortic valves of healthy patients. The authors
10
11 proposed that the mineral spheres are the first mineralized structures formed in cardiovascular
12
13 tissues. Their diameters, about 500 nm for healthy patients, are very close to those measured
14
15 here for the calcified vesicles in kidneys (~ 400 nm). The size of cardiovascular mineral spheres
16
17 increases with the disease severity (larger diameters are about 1 μm). Interestingly, these
18
19 spheres present striking similarities with those found in lithiasic kidneys⁶⁵ including their sizes
20
21 (about 1 μm) and morphologies (multilayered with alternating organic and mineral materials).
22
23 The calcified vesicles observed here are probably a less evolved stage of these calcifications.
24
25
26
27
28

29 From all these results, we propose that the calcified vesicles correspond to the early
30
31 stages of mineral deposition and that they are able to grow under the effect of factors promoting
32
33 mineralization. Many factors have been reported to be involved in the pathological evolution
34
35 of RPs.⁵⁶ In cardiovascular tissues, it was suggested that mineral spheres may trigger an
36
37 osteoblastic transdifferentiation of cardiovascular cells, similarly to subcutaneous and
38
39 intramuscular implantations of calcium phosphates that are able to induce cells mineralizing
40
41 phenotype and to drive bone formation.³ The role of large MPs remains unclear whether they
42
43 stay nanometric or they play a role in the formation of macroscopic RPs. Interestingly, large
44
45 MPs with carbonate in their core have a higher calcium content compared to pure calcium
46
47 phosphate MPs (calcium edge in Figure 7) suggesting that the presence of carbonate could favor
48
49 a higher mineral deposition.
50
51
52
53
54
55
56
57
58
59
60

CONCLUSION

In conclusion, this work consists of a systematic nanocharacterization of the morphologies and chemical compositions of incipient RPs in human kidney. Our analysis shows that the incipient calcifications present a high diversity in terms of size (nanometric or micrometric), morphology and chemical composition (calcium phosphate and carbonate). We have identified two main types of nano-calcifications: calcified vesicles and large MPs, most of them containing carbonate in their core similarly to the bone mineral precursors. These results tend to show that the nucleation of the early mineral can start in kidney *via* at least two different mechanisms: a carbonate precursor acting as a bioseed or the interaction with organic compounds. At larger scales, micro-calcifications appear to be composed, at least partly, of calcified vesicles embedded in an organic fibrillary matrix the nature of which is still unknown. Further works will be dedicated in particular to unveil the nature of the organic matrix found in micro-calcifications, the carbonate-containing MPs, the calcified vesicles and the cells producing them. Interestingly, these objects present striking similarities with the calcified structures reported in physiological bone and pathological cardiovascular biominerals, suggesting that common mechanisms could be responsible for the appearance of RPs and physiological biominerals.

From a general point of view, the present strategy is of great interest to be used as a systematic tool for the investigation of pathological biominerals. In most cases, quantitative data are missing and the complexity of the system does not allow to propose a simple model for their formation. Our study demonstrates that STEM-EELS provides analytical data allowing a reliable comparison between the different biominerals. The determination of the mineral/organic interface at the nanoscale and its comparison with other systems more widely

1
2
3 studied and better understood constitutes an essential first step for the understanding of the
4
5 underlying mechanisms and for proposing formation models.
6
7
8
9
10
11
12
13
14
15
16
17
18
19
20
21
22
23
24
25
26
27
28
29
30
31
32
33
34
35
36
37
38
39
40
41
42
43
44
45
46
47
48
49
50
51
52
53
54
55
56
57
58
59
60

EXPERIMENTAL SECTION

Kidney stones, papillae sections and reference compounds

Macroscopic kidney stones composed of carbonated hydroxyapatite, amorphous carbonated calcium phosphate and whitlockite were obtained from Tenon Hospital. Synthetic hydroxyapatite purchased from Biorad and calcite were used as reference compounds for EELS analysis to determine the composition of stones and calcifications in papillae sections. Reference compounds and kidney stones were ground in an agate mortar and suspended in pure ethanol before deposition onto TEM holey-carbon copper grids.

Papillae were collected from human kidneys removed because of cancer as previously described.¹⁴ Patients gave a written consent in the Urology Unit relative to kidney removal and tissue conservation but not to the use of clinical or biological data. Papillae were therefore anonymously collected and no data relative to patients were recorded, in accord with French legislation and the Helsinki Declaration for Patient Safety. Part of each papilla was first analyzed by von Kossa staining to check for the presence of RPs in the specimen (details in ¹⁴). Two papillae from two non-stone formers were selected for the present study. Small pieces of each papilla were kept for TEM and STEM analysis. For electron microscopy analysis, papilla specimens were chemically fixed with 2.5% glutaraldehyde in 0.1 mM sodium cacodylate buffer and post-fixed with 1.0% OsO₄. They were then dehydrated and embedded in epoxy resin (EMbed 812). Ultrathin sections (80 nm) were stained with uranyl acetate and deposited on a bare copper grid without carbon film to avoid this contribution during the EELS acquisitions.

FTIR analysis

The composition of the kidney stones was determined at the Tenon Hospital using an FTIR spectrometer (Vector 22; Bruker Spectrospin, Wissembourg, France) according to a previously described analytical protocol.⁵ Data were collected in the absorption mode between 4,000 and 400 cm^{-1} with a resolution of 4 cm^{-1} .

STEM-EELS and EDX acquisitions and data processing

Specimens were first screened using a Philips CM10 electron microscope to identify the regions of interest. High-angle annular dark-field images (HAADF) and EELS data were then acquired using a VG HB501 STEM equipped with a cold field emission gun, operated at 100 keV. To minimise the beam radiation damage, samples were liquid-nitrogen cooled to approximately 170 K using a home-made cryo-stage. EELS data were collected on a low-noise, low-temperature CCD camera (Princeton Instruments) optically coupled to a scintillator in the image plane of a Gatan 666 magnetic sector. The convergence and collection half-angles were 7 mrad and 22 mrad respectively. Core-loss spectra were acquired in the energy range corresponding to characteristic edges for the elements of interest (U, P, C, Ca, N, O), using the spectrum-imaging (SI) mode⁶⁶ with an energy dispersion of 0.5 eV/channel. Typical energy resolution was about 1 to 1.5 eV and the beam diameter was estimated as 1 nm.

In the SI mode, the focused beam is scanned over a region of interest and a whole spectrum is acquired at each position of the scan. Such a hyperspectral image contains typically 10000 spectra. These spectra could be processed individually. This is usually performed by removing the background and summing the intensity corresponding to a characteristic edge and thus building elemental maps. Because this data set contains a lot of redundant information, it is more efficient to process it as a whole using multivariate statistical techniques.⁶⁷ We used

1
2
3 Hyperspy, an open-source software suite ⁶⁸ for principal component analysis (PCA) as a
4 filtering method for separating meaningful signal components from noise, in particular for
5 acquisitions at lower doses when the signal-to-noise ratio was poor. For the carbon K-edge,
6 multi-Gaussian fitting was performed using the NLLS (non-linear least squares) method in
7 Gatan's Digital Micrograph software.
8
9
10
11
12
13
14

15 Energy dispersive X-ray spectroscopy (EDX) analysis was carried out in STEM mode in an
16 FEI Titan Themis 200 TEM/STEM operated at 200 keV and fitted with a Chemistem Super-X
17 EDX spectrometer comprising four separate windowless detectors placed symmetrically around
18 the sample. Quantitative maps were acquired using the Bruker ESPRIT v.1.9 software with an
19 acquisition time of about 20-30 min for total area. The element ratios were calculated with the
20 Interactive TEM algorithm based on the Cliff-Lorimer method. The K factors were determined
21 experimentally from a standard specimen of tricalcium phosphate (Prolabo) under the same
22 experimental conditions as for the kidney specimens.
23
24
25
26
27
28
29
30
31
32
33
34
35
36
37
38
39
40
41
42
43
44
45
46
47
48
49
50
51
52
53
54
55
56
57
58
59
60

1
2
3 ASSOCIATED CONTENT
4
5
6
7

8
9 SUPPORTING INFORMATION
10
11

12 The Supporting Information is available free of charge on the ACS Publications website at

13
14 DOI:

15
16
17 FTIR analysis of kidney stones. Electron dose effect on EELS features for mineral, organic
18 compounds and resin. EELS fingerprints for organic compounds and resin. Table containing
19 the EELS characteristic features for mineral, organic compounds and resin (PDF).
20
21
22
23
24
25

26
27 ACKNOWLEDGMENTS
28

29 We would like to thank Dr. V. Frochot for his preliminary experiments and useful discussions.

30 We are grateful to C. Colliex for its constructive critiques and its helpful corrections of an early
31 version of this work.
32
33

34
35
36 This work was partially funded *via* the CNRS-CEA “METSA” French network (FR CNRS
37 3507) and the EU grant No. 312483-ESTEEM2.
38
39
40
41
42
43
44
45
46
47
48
49
50
51
52
53
54
55
56
57
58
59
60

REFERENCES

- 1
- 2
- 3
- 4
- 5
- 6
- 7 (1) Bonucci, E. *Biological Calcification: Normal and Pathological Processes in the Early Stages*; Springer-Verlag: Berlin Heidelberg, 2007.
- 8
- 9 (2) Bazin, D.; Daudon, M.; Combes, C.; Rey, C. Characterization and Some Physicochemical
- 10 Aspects of Pathological Microcalcifications. *Chem. Rev.* **2012**, *112*, 5092–5120.
- 11 (3) Bertazzo, S.; Gentleman, E.; Cloyd, K. L.; Chester, A. H.; Yacoub, M. H.; Stevens, M. M. Nano-
- 12 Analytical Electron Microscopy Reveals Fundamental Insights into Human Cardiovascular
- 13 Tissue Calcification. *Nat. Mater.* **2013**, *12*, 576–583.
- 14 (4) Daudon, M.; Jungers, P.; Bazin, D. Peculiar Morphology of Stones in Primary Hyperoxaluria. *N.*
- 15 *Engl. J. Med.* **2008**, *359*, 100–102.
- 16 (5) Estepa, L.; Daudon, M. Contribution of Fourier Transform Infrared Spectroscopy to the
- 17 Identification of Urinary Stones and Kidney Crystal Deposits. *Biospectroscopy* **1998**, *3*, 347–
- 18 369.
- 19 (6) Daudon, M.; Bader, C. A.; Jungers, P. Urinary Calculi: Review of Classification Methods and
- 20 Correlations with Etiology. *Scanning Microsc.* **1993**, *7*, 1081–1106.
- 21 (7) Daudon, M.; Jungers, P. Stone Composition and Morphology: A Window on Etiology. In
- 22 *Urolithiasis*; Springer, London, 2012; pp 113–140.
- 23 (8) Khan, S. R.; Pearle, M. S.; Robertson, W. G.; Gambaro, G.; Canales, B. K.; Doizi, S.; Traxer, O.;
- 24 Tiselius, H.-G. Kidney Stones. *Nat. Rev. Dis. Primer* **2016**, *2*, 16008.
- 25 (9) Letavernier, E.; Bazin, D.; Daudon, M. Randall’s Plaque and Kidney Stones: Recent Advances
- 26 and Future Challenges. *Comptes Rendus Chim.* **2016**, *19*, 1456–1460.
- 27 (10) Evan, A. P.; Worcester, E. M.; Coe, F. L.; Williams, J.; Lingeman, J. E. Mechanisms of Human
- 28 Kidney Stone Formation. *Urolithiasis* **2015**, *43*, 19–32.
- 29 (11) Randall, A. An Hypothesis for the Origin of Renal Calculus. *N. Engl. J. Med.* **1936**, *214*, 234–
- 30 242.
- 31 (12) Randall, A. The Origin and Growth of Renal Calculi. *Ann. Surg.* **1937**, *105*, 1009–1027.
- 32 (13) O’Kell, A. L.; Lovett, A. C.; Canales, B. K.; Gower, L. B.; Khan, S. R. Development of a Two-Stage
- 33 Model System to Investigate the Mineralization Mechanisms Involved in Idiopathic Stone
- 34 Formation: Stage 2 *In Vivo* Studies of Stone Growth on Biomimetic Randall’s Plaque.
- 35 *Urolithiasis* **2018**, *47*, 335–346.
- 36 (14) Verrier, C.; Bazin, D.; Huguet, L.; Stéphan, O.; Gloter, A.; Verpont, M.-C.; Frochot, V.; Haymann,
- 37 J.-P.; Brocheriou, I.; Traxer, O.; Daudon, M.; Letavernier, E. Topography, Composition and
- 38 Structure of Incipient Randall Plaque at the Nanoscale Level. *J. Urol.* **2016**, *196*, 1566–1574.
- 39 (15) Daudon, M.; Traxer, O.; Jungers, P.; Bazin, D. Stone Morphology Suggestive of Randall’s
- 40 Plaque. *AIP Conf. Proc.* **2007**, *900*, 26–34.
- 41 (16) Kłosowski, M. M.; Friederichs, R. J.; Nichol, R.; Antolin, N.; Carzaniga, R.; Windl, W.; Best, S. M.;
- 42 Shefelbine, S. J.; McComb, D. W.; Porter, A. E. Probing Carbonate in Bone Forming Minerals on
- 43 the Nanometre Scale. *Acta Biomater.* **2015**, *20*, 129–139.
- 44 (17) Nitiputri, K.; Ramasse, Q. M.; Autefage, H.; McGilvery, C. M.; Boonrungsiman, S.; Evans, N. D.;
- 45 Stevens, M. M.; Porter, A. E. Nanoanalytical Electron Microscopy Reveals a Sequential
- 46 Mineralization Process Involving Carbonate-Containing Amorphous Precursors. *ACS Nano*
- 47 **2016**, *10*, 6826–6835.
- 48 (18) Boonrungsiman, S.; Gentleman, E.; Carzaniga, R.; Evans, N. D.; McComb, D. W.; Porter, A. E.;
- 49 Stevens, M. M. The Role of Intracellular Calcium Phosphate in Osteoblast-Mediated Bone
- 50 Apatite Formation. *Proc. Natl. Acad. Sci.* **2012**, *109*, 14170–14175.
- 51 (19) Srot, V.; Bussmann, B.; Salzberger, U.; Deuschle, J.; Watanabe, M.; Pokorny, B.; Jelenko
- 52 Turinek, I.; Mark, A. F.; van Aken, P. A. Magnesium-Assisted Continuous Growth of Strongly
- 53 Iron-Enriched Incisors. *ACS Nano* **2017**, *11*, 239–248.
- 54
- 55
- 56
- 57
- 58
- 59
- 60

- 1
2
3 (20) Srot, V.; Wegst, U. G. K.; Salzberger, U.; Koch, C. T.; Hahn, K.; Kopold, P.; van Aken, P. A.
4 Microstructure, Chemistry, and Electronic Structure of Natural Hybrid Composites in Abalone
5 Shell. *Micron* **2013**, *48*, 54–64.
- 6 (21) Mahamid, J.; Sharir, A.; Addadi, L.; Weiner, S. Amorphous Calcium Phosphate Is a Major
7 Component of the Forming Fin Bones of Zebrafish: Indications for an Amorphous Precursor
8 Phase. *Proc. Natl. Acad. Sci.* **2008**, *105*, 12748–12753.
- 9 (22) Maruotti, N.; Corrado, A.; Cantatore, F. P. Osteoblast Role in Osteoarthritis Pathogenesis. *J.*
10 *Cell. Physiol.* **2017**, *232*, 2957–2963.
- 11 (23) Scimeca, M.; Bonfiglio, R.; Varone, F.; Ciuffa, S.; Mauriello, A.; Bonanno, E. Calcifications in
12 Prostate Cancer: An Active Phenomenon Mediated by Epithelial Cells with Osteoblast-
13 Phenotype. *Microsc. Res. Tech.* **2018**, *81*, 745–748.
- 14 (24) Evan, A. P.; Coe, F. L.; Rittling, S. R.; Bledsoe, S. M.; Shao, Y.; Lingeman, J. E.; Worcester, E. M.
15 Apatite Plaque Particles in Inner Medulla of Kidneys of Calcium Oxalate Stone Formers:
16 Osteopontin Localization. *Kidney Int.* **2005**, *68*, 145–154.
- 17 (25) Khan, S. R.; Rodriguez, D. E.; Gower, L. B.; Monga, M. Association of Randall Plaque with
18 Collagen Fibers and Membrane Vesicles. *J. Urol.* **2012**, *187*, 1094–1100.
- 19 (26) Cosmidis, J.; Benzerara, K.; Nassif, N.; Tyliczszak, T.; Bourdelle, F. Characterization of Ca-
20 Phosphate Biological Materials by Scanning Transmission X-Ray Microscopy (STXM) at the Ca
21 L_{2,3}-, P L_{2,3}- and C K-Edges. *Acta Biomater.* **2015**, *12*, 260–269.
- 22 (27) Dorozhkin, S. V.; Epple, M. Biological and Medical Significance of Calcium Phosphates. *Angew.*
23 *Chem. Int. Ed.* **2002**, *41*, 3130–3146.
- 24 (28) Benzerara, K.; Yoon, T. H.; Tyliczszak, T.; Constantz, B.; Spormann, A. M.; Brown, G. E. Scanning
25 Transmission X-Ray Microscopy Study of Microbial Calcification. *Geobiology* **2004**, *2*, 249–259.
- 26 (29) Brandes, J. A.; Wirick, S.; Jacobsen, C. Carbon K-Edge Spectra of Carbonate Minerals. *J.*
27 *Synchrotron Radiat.* **2010**, *17*, 676–682.
- 28 (30) DeVol, R. T.; Sun, C.-Y.; Marcus, M. A.; Coppersmith, S. N.; Myneni, S. C. B.; Gilbert, P. U. P. A.
29 Nanoscale Transforming Mineral Phases in Fresh Nacre. *J. Am. Chem. Soc.* **2015**, *137*, 13325–
30 13333.
- 31 (31) Rajendran, J.; Gialanella, S.; Aswath, P. B. XANES Analysis of Dried and Calcined Bones. *Mater.*
32 *Sci. Eng. C* **2013**, *33*, 3968–3979.
- 33 (32) Gregori, G.; Kleebe, H.-J.; Mayr, H.; Ziegler, G. EELS Characterisation of β -Tricalcium Phosphate
34 and Hydroxyapatite. *J. Eur. Ceram. Soc.* **2006**, *26*, 1473–1479.
- 35 (33) Kruse, J.; Leinweber, P.; Eckhardt, K.-U.; Godlinski, F.; Hu, Y.; Zuin, L. Phosphorus L_{2,3}-Edge
36 XANES: Overview of Reference Compounds. *J. Synchrotron Radiat.* **2009**, *16*, 247–259.
- 37 (34) Maginot, M.; Lin, S.; Liu, Y.; Yuan, B.; Feng, J. Q.; Aswath, P. B. The *In Vivo* Role of DMP-1 and
38 Serum Phosphate on Bone Mineral Composition. *Bone* **2015**, *81*, 602–613.
- 39 (35) de Groot, F. M. F.; Fuggle, J. C.; Thole, B. T.; Sawatzky, G. A. 2p X-Ray Absorption of 3D
40 Transition-Metal Compounds: An Atomic Multiplet Description Including the Crystal Field.
41 *Phys. Rev. B* **1990**, *42*, 5459–5468.
- 42 (36) Goode, A. E.; Porter, A. E.; Ryan, M. P.; McComb, D. W. Correlative Electron and X-Ray
43 Microscopy: Probing Chemistry and Bonding with High Spatial Resolution. *Nanoscale* **2015**, *7*,
44 1534–1548.
- 45 (37) Mann, S. *Biomineralization: Principles and Concepts in Bioinorganic Materials Chemistry*;
46 Oxford University Press: Oxford, 2001.
- 47 (38) Beniash, E.; Metzler, R. A.; Lam, R. S. K.; Gilbert, P. U. P. A. Transient Amorphous Calcium
48 Phosphate in Forming Enamel. *J. Struct. Biol.* **2009**, *166*, 133–143.
- 49 (39) Landis, W. J.; Pains, M. C.; Hodgens, K. J.; Glimcher, M. J. Matrix Vesicles in Embryonic Chick
50 Bone: Considerations of Their Identification, Number, Distribution, and Possible Effects on
51 Calcification of Extracellular Matrices. *J. Ultrastruct. Mol. Struct. Res.* **1986**, *95*, 142–163.
- 52 (40) Mahamid, J.; Sharir, A.; Gur, D.; Zelzer, E.; Addadi, L.; Weiner, S. Bone Mineralization Proceeds
53 through Intracellular Calcium Phosphate Loaded Vesicles: A Cryo-Electron Microscopy Study. *J.*
54 *Struct. Biol.* **2011**, *174*, 527–535.
- 55
56
57
58
59
60

- 1
2
3 (41) Golub, E. E. Role of Matrix Vesicles in Biomineralization. *Biochim. Biophys. Acta* **2009**, *1790*,
4 1592–1598.
- 5 (42) Weiner, S. Biomineralization: A Structural Perspective. *J. Struct. Biol.* **2008**, *163*, 229–234.
- 6 (43) Letavernier, E.; Kauffenstein, G.; Huguet, L.; Navasiolava, N.; Boudierlique, E.; Tang, E.;
7 Delaitre, L.; Bazin, D.; Frutos, M. de; Gay, C.; Perez, J.; Verpont, M.-C.; Haymann, J.-P.; Pomozi,
8 V.; Zoll, J.; Saux, O. L.; Daudon, M.; Leftheriotis, G.; Martin, L. ABCC6 Deficiency Promotes
9 Development of Randall Plaque. *J. Am. Soc. Nephrol.* **2018**, *29*, 2337–2347.
- 10 (44) Jia, Z.; Wang, S.; Tang, J.; He, D.; Cui, L.; Liu, Z.; Guo, B.; Huang, L.; Lu, Y.; Hu, H. Does Crystal
11 Deposition in Genetic Hypercalciuric Rat Kidney Tissue Share Similarities With Bone
12 Formation? *Urology* **2014**, *83*, 509.e7-509.e14.
- 13 (45) Khan, S. R.; Gambaro, G. Role of Osteogenesis in the Formation of Randall's Plaques. *Anat.*
14 *Rec. Hoboken NJ 2007* **2016**, *299*, 5–7.
- 15 (46) Crane, N. J.; Popescu, V.; Morris, M. D.; Steenhuis, P.; Ignelzi, M. A. Raman Spectroscopic
16 Evidence for Octacalcium Phosphate and Other Transient Mineral Species Deposited during
17 Intramembranous Mineralization. *Bone* **2006**, *39*, 434–442.
- 18 (47) Pan, H.; Darvell, B. W. Effect of Carbonate on Hydroxyapatite Solubility. *Cryst. Growth Des.*
19 **2010**, *10*, 845–850.
- 20 (48) Wang, Y.; Euw, S. V.; Laurent, G.; Crevant, C.; Bonhomme-Courty, L.; Giraud-Guille, M.-M.;
21 Babonneau, F.; Nassif, N.; Azaïs, T. Impact of Collagen Confinement vs. Ionic Substitutions on
22 the Local Disorder in Bone and Biomimetic Apatites. *Mater. Horiz.* **2014**, *1*, 224–231.
- 23 (49) Müller, W. E. G.; Schröder, H. C.; Schlossmacher, U.; Grebenjuk, V. A.; Ushijima, H.; Wang, X.
24 Induction of Carbonic Anhydrase in SaOS-2 Cells, Exposed to Bicarbonate and Consequences
25 for Calcium Phosphate Crystal Formation. *Biomaterials* **2013**, *34*, 8671–8680.
- 26 (50) Tournus, M.; Seguin, N.; Perthame, B.; Thomas, S. R.; Edwards, A. A Model of Calcium
27 Transport along the Rat Nephron. *Am. J. Physiol.-Ren. Physiol.* **2013**, *305*, F979–F994.
- 28 (51) Purkerson, J. M.; Schwartz, G. J. The Role of Carbonic Anhydrases in Renal Physiology. *Kidney*
29 *Int.* **2007**, *71*, 103–115.
- 30 (52) Obrador, G.; Yuan, H.; Shih, T. M.; Wang, Y. H.; Shia, M. A.; Alexander, E. A.; Schwartz, J. H.
31 Characterization of Anion Exchangers in an Inner Medullary Collecting Duct Cell Line. *J. Am.*
32 *Soc. Nephrol.* **1998**, *9*, 746–754.
- 33 (53) Daudon, M.; Bazin, D.; Letavernier, E. Randall's Plaque as the Origin of Calcium Oxalate Kidney
34 Stones. *Urolithiasis* **2015**, *43*, 5–11.
- 35 (54) Nudelman, F.; Pieterse, K.; George, A.; Bomans, P. H. H.; Friedrich, H.; Brylka, L. J.; Hilbers, P.
36 A. J.; de With, G.; Sommerdijk, N. A. J. M. The Role of Collagen in Bone Apatite Formation in
37 the Presence of Hydroxyapatite Nucleation Inhibitors. *Nat. Mater.* **2010**, *9*, 1004–1009.
- 38 (55) Flade, K.; Lau, C.; Mertig, M.; Pompe, W. Osteocalcin-Controlled Dissolution–Reprecipitation
39 of Calcium Phosphate under Biomimetic Conditions. *Chem. Mater.* **2001**, *13*, 3596–3602.
- 40 (56) Khan, S. R.; Canales, B. K. Unified Theory on the Pathogenesis of Randall's Plaques and Plugs.
41 *Urolithiasis* **2015**, *43 Suppl 1*, 109–123.
- 42 (57) Shapiro, I. M.; Landis, W. J.; Risbud, M. V. Matrix Vesicles: Are They Anchored Exosomes?
43 *Bone* **2015**, *79*, 29–36.
- 44 (58) Mahamid, J.; Aichmayer, B.; Shimoni, E.; Ziblat, R.; Li, C.; Siegel, S.; Paris, O.; Fratzl, P.; Weiner,
45 S.; Addadi, L. Mapping Amorphous Calcium Phosphate Transformation into Crystalline Mineral
46 from the Cell to the Bone in Zebrafish Fin Rays. *Proc. Natl. Acad. Sci.* **2010**, *107*, 6316–6321.
- 47 (59) Reynolds, J. L.; Skepper, J. N.; McNair, R.; Kasama, T.; Gupta, K.; Weissberg, P. L.; Jahnen-
48 Dechent, W.; Shanahan, C. M. Multifunctional Roles for Serum Protein Fetuin-A in Inhibition of
49 Human Vascular Smooth Muscle Cell Calcification. *J. Am. Soc. Nephrol.* **2005**, *16*, 2920–2930.
- 50 (60) Cui, L.; Houston, D. A.; Farquharson, C.; MacRae, V. E. Characterisation of Matrix Vesicles in
51 Skeletal and Soft Tissue Mineralisation. *Bone* **2016**, *87*, 147–158.
- 52 (61) Wuthier, R. E.; Eanes, E. D. Effect of Phospholipids on the Transformation of Amorphous
53 Calcium Phosphate to Hydroxyapatite *In Vitro*. *Calcif. Tissue Res.* **1975**, *19*, 197–210.
- 54
55
56
57
58
59
60

- 1
2
3 (62) Skrtic, D.; Eanes, E. D. Membrane-Mediated Precipitation of Calcium Phosphate in Model
4 Liposomes with Matrix Vesicle-Like Lipid Composition. *Bone Miner.* **1992**, *16*, 109–119.
- 5 (63) Wiesmann, H. P.; Meyer, U.; Plate, U.; Höhling, H. J. Aspects of Collagen Mineralization in Hard
6 Tissue Formation. *Int. Rev. Cytol.*, **2004**, *242*, 121–156.
- 7 (64) Basalyga, D. M.; Simionescu, D. T.; Xiong, W.; Baxter, B. T.; Starcher, B. C.; Vyavahare, N. R.
8 Elastin Degradation and Calcification in an Abdominal Aorta Injury Model: Role of Matrix
9 Metalloproteinases. *Circulation* **2004**, *110*, 3480–3487.
- 10 (65) Evan, A. P.; Lingeman, J. E.; Coe, F. L.; Parks, J. H.; Bledsoe, S. B.; Shao, Y.; Sommer, A. J.;
11 Paterson, R. F.; Kuo, R. L.; Grynopas, M. Randall's Plaque of Patients with Nephrolithiasis Begins
12 in Basement Membranes of Thin Loops of Henle. *J. Clin. Invest.* **2003**, *111*, 607–616.
- 13 (66) Jeanguillaume, C.; Colliex, C.; Ballongue, P.; Teneé, M. New STEM Multisignal Imaging Modes,
14 Made Accessible through the Evaluation of Detection Efficiencies. *Ultramicroscopy* **1992**, *45*,
15 205–217.
- 16 (67) de la Peña, F.; Berger, M.-H.; Hochepped, J.-F.; Dynys, F.; Stephan, O.; Walls, M. Mapping
17 Titanium and Tin Oxide Phases Using EELS: An Application of Independent Component
18 Analysis. *Ultramicroscopy* **2011**, *111*, 169–176.
- 19 (68) Francisco de la Peña; Eric Prestat; Vidar Tonaas Fauske; Pierre Burdet; Petras Jokubauskas;
20 Magnus Nord; Tomas Ostasevicius; Katherine E. MacArthur; Mike Sarahan; Duncan N.
21 Johnstone; Joshua Taillon; Jonas Lähnemann; Vadim Migunov; Alberto Eljarrat; Jan Caron;
22 Thomas Aarholt; Stefano Mazzucco; Michael Walls; Tom Slater; Florian Winkler; *et al.*
23 *Hyperspy/Hyperspy: HyperSpy v1.5.2*; Zenodo, 2019.
24
25
26
27
28
29
30
31
32
33
34
35
36
37
38
39
40
41
42
43
44
45
46
47
48
49
50
51
52
53
54
55
56
57
58
59
60